Accelerated Publications

Solution Structure of *Pyrococcus furiosus* RPP21, a Component of the Archaeal RNase P Holoenzyme, and Interactions with Its RPP29 Protein Partner[†]

Carlos D. Amero,[‡] William P. Boomershine,[§] Yiren Xu,[§] and Mark Foster*[,‡,§]

Biophysics Program, Center for RNA Biology and Department of Biochemistry, The Ohio State University, Columbus, Ohio 43210

Received August 25, 2008; Revised Manuscript Received September 26, 2008

ABSTRACT: RNase P is the ubiquitous ribonucleoprotein metalloenzyme responsible for cleaving the 5′-leader sequence of precursor tRNAs during their maturation. While the RNA subunit is catalytically active on its own at high monovalent and divalent ion concentrations, four protein subunits are associated with archaeal RNase P activity in vivo: RPP21, RPP29, RPP30, and POP5. These proteins have been shown to function in pairs: RPP21−RPP29 and POP5−RPP30. We have determined the solution structure of RPP21 from the hyperthermophilic archaeon *Pyrococcus furiosus* (*Pfu*) using conventional and paramagnetic NMR techniques. *Pfu* RPP21 in solution consists of an unstructured N-terminus, two α-helices, a zinc binding motif, and an unstructured C-terminus. Moreover, we have used chemical shift perturbations to characterize the interaction of RPP21 with RPP29. The data show that the primary contact with RPP29 is localized to the two helices of RPP21. This information represents a fundamental step toward understanding structure−function relationships of the archaeal RNase P holoenzyme.

Ribonuclease P (RNase P) is a ribonucleoprotein enzyme that is essential in all three domains of life for cleaving the 5′-leader sequence of precursor tRNA molecules (ptRNA)[1] (*1−3*). In archaea, the catalytic RNA subunit (RPR) is associated with four protein subunits (RPPs) homologous to four eukaryotic nuclear RNase P proteins: RPP21, RPP29, RPP30, and POP5 (*4*). For RNase P from the hyperthermophilic archaeon *Pyrococcus furiosus* (*Pfu*), robust ptRNA cleavage activity can be reconstituted from in vitro assembly of transcribed RPR and the four recombinantly expressed and purified RPPs (*5*). These four proteins function in pairs (*5*), as the RPP21−RPP29 and RPP30−POP5 heterodimers can activate the RNA subunit at relatively low salt concentrations, while addition of either RPP21 or RPP29 to the RPP30−POP5 pair (or vice versa) does not significantly increase activity. These reconstitution data, together with the results from yeast two-hybrid experiments on archaeal and yeast homologues (*6−8*), suggest that RPP21 and RPP29 (as well as RPP30 and POP5) associate to promote RNase P holoenzyme assembly. Furthermore, recombinantly expressed human RPP21 was found to bind ptRNA (*9*), and RPP21 and RPP29 together were shown to functionally reconstitute the activity of human RNase P RNA (*10*), underscoring the evolutionary conservation of these important protein−protein and protein−RNA interactions. To gain insight into the structure and function of the RNase P holoenzyme, we have been investigating the three-dimensional structures of the individual subunits and report here the solution structure of *Pfu* RPP21.

Pfu RPP21 is a 117-residue protein that is highly conserved both within and between Archaea and Eukarya (Figure 1). Sequence analysis suggested that the protein contains a zinc ribbon motif (*11*) featuring four invariant cysteine residues. Determination of the *Pfu* RPP21 structure is an important step toward a structural model of the RNase P holoenzyme. Previously, we determined the solution structure of *Methanothermobacter thermautotrophicus* RPP29 by NMR (*12*) and the structure of *Pfu* POP5 by X-ray crystallography (*13*). The crystal structures of *P. horikoshii* (*Pho*) Pop5 and RPP30 (*14, 15*) and RPP21 (*16*) have also been reported. While determining the structures of the individual RPPs represents a crucial step in understanding their roles within the holoenzyme, establishing how they interact with each other will provide greater insight into their role in RNA catalysis.

We determined the solution structure of *Pfu* RPP21 by applying conventional and state-of-the-art paramagnetic NMR spectroscopy (*17*). Taking advantage of the metal

---

[†] This work was supported by a grant from the National Institutes of Health (GM67807) to M.F. and V. Gopalan (The Ohio State University).

* To whom correspondence should be addressed: Department of Biochemistry, The Ohio State University, 734 Riffe Building, 484 W. 12th Ave., Columbus, OH 43210. Telephone: (614) 292-1377. Fax: (614) 292-6773. E-mail: foster.281@osu.edu.

[‡] Biophysics Program.

[§] Department of Biochemistry.

[1] Abbreviations: NMR, nuclear magnetic resonance; TROSY, transverse relaxation optimized spectroscopy; HSQC, heteronuclear single-quantum correlation spectroscopy; NOE, nuclear Overhauser effect; PCS, pseudochemical shifts; *Pfu*, *Pyrococcus furiosus; Pho, P. horikoshii*; RPP, RNase P protein; RPR, RNase P RNA; ptRNA, precursor tRNA.

10.1021/bi8015982 CCC: $40.75

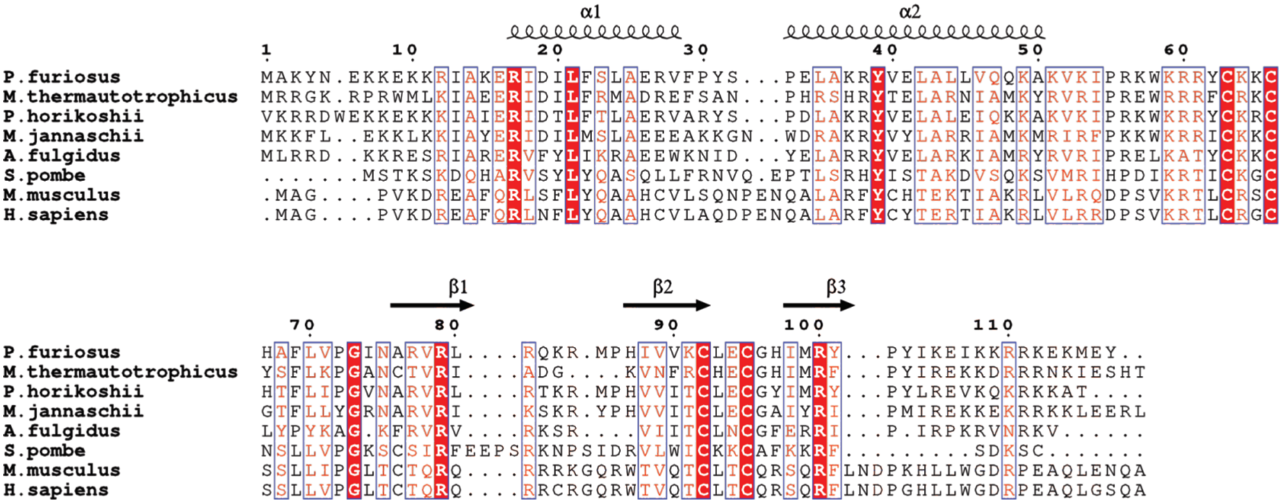

FIGURE 1: Sequence alignment of RPP21 homologues from Archaea and Eukarya. The alignment was generated with CLUSTALW (*47*). Red lettering indicates a global similarity score of 0.7, while red boxes indicate invariant residues. Secondary structural elements observed in the NMR ensemble are indicated in cartoon format. The aligned sequences are from *P. furiosus* (NCBI entry NP_579342), *M. thermautotrophicus* (NCBI entry NP_276730), *P. horikoshii* (NCBI entry NP_143456), *Methanocaldococcus jannaschii* (NCBI entry NP_247957), *Archaeoglobus fulgidus* (NCBI entry NP_068950), *Schizosaccharomyces pombe* (NCBI entry NP_596472), *Mus musculus* (NCBI entry NP_080584), and *Homo sapiens* (NCBI entry NP_079115). *Pfu* RPP21 belongs to pfam04032. This figure was generated with ESPRIPT (*48*).

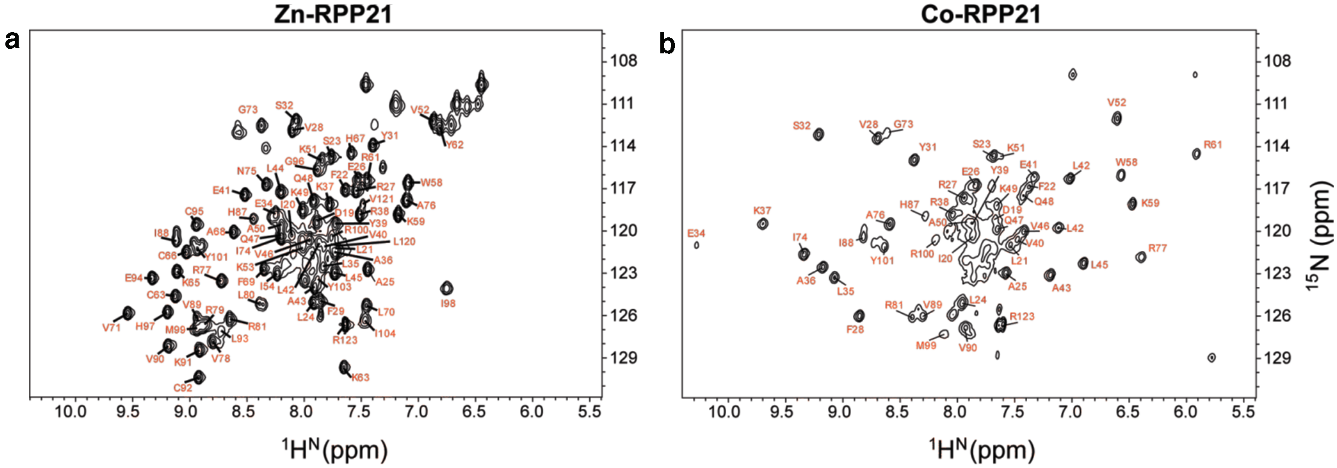

FIGURE 2: Two-dimensional ^{1}H−^{15}N NMR spectra of *Pfu* RPP21. Backbone amide assignments are as indicated: (a) zinc-reconstituted RPP21 and (b) cobalt-reconstituted RPP21.

binding properties of *Pfu* RPP21, we replaced the diamagnetic Zn^{2+} with the paramagnetic Co^{2+}, which provided a unique set of restraints otherwise unavailable (*18*). Furthermore, to provide insight into the interactions between RPP21 and RPP29, chemical shift perturbations (*19, 20*) were utilized to determine which residues in RPP21 are responsible for interactions with RPP29. These data have allowed us to identify residues within RPP21 that interact with RPP29 in the absence of the RNA, facilitating interpretation of functional defects obtained from alanine scanning mutagenesis (*16*). This work represents an important step toward a model of the assembly and structure of the RNase P holoenzyme from archaea and eukaryotes.

MATERIALS AND METHODS

Protein Expression and Purification. The gene encoding *Pfu* RPP21 was amplified by PCR from genomic DNA as the template and gene-specific DNA primers (forward, 5′-GCT AAA TAC AAT GAG AAA AAA GAA AAA AAG **CGT** ATT G; reverse, 5′-C TAG CTC GAG gct gcc gcg cgg cac cag acc acc ATA TTC CAT TTT TTC TTT TCT TCT C; an *Xho*I restriction site is underlined, the C-terminal Gly-Gly linker and thrombin cleavage site, Leu-Val-Pro-Arg-Gly-Ser, are in lowercase letters, and nucleotides altered to improve codon usage for *Escherichia coli* are in bold) and then subcloned into the pET-33b vector (Novagen, Inc.). The recombinant protein was overexpressed in *E. coli* Rosetta (DE3) cells (Novagen, Inc.) grown at 37 °C in minimal M9 medium containing 1 g/L [^{15}N]ammonium chloride and 2 g/L [^{13}C]glucose as the sole nitrogen and carbon sources, respectively, and supplemented with 30 μg/L kanamycin and 34 μg/L chloramphenicol. Production of RPP21 was induced by addition of 1 mM isopropyl β-D-thiogalactoside (IPTG) and 50 μM zinc chloride when the cells reached an OD$_{600}$ of ≈0.6, and the cells were harvested after 4 h by centrifugation. Cells were suspended in denaturing lysis buffer [50 mM Tris (pH 7.4), 50 mM KCl, 5 mM imidazole, and 6 M guanidine-HCl] and lysed by sonication. The protein was purified using a three-step purification protocol. In the first step, affinity chromatography was performed using a 5 mL

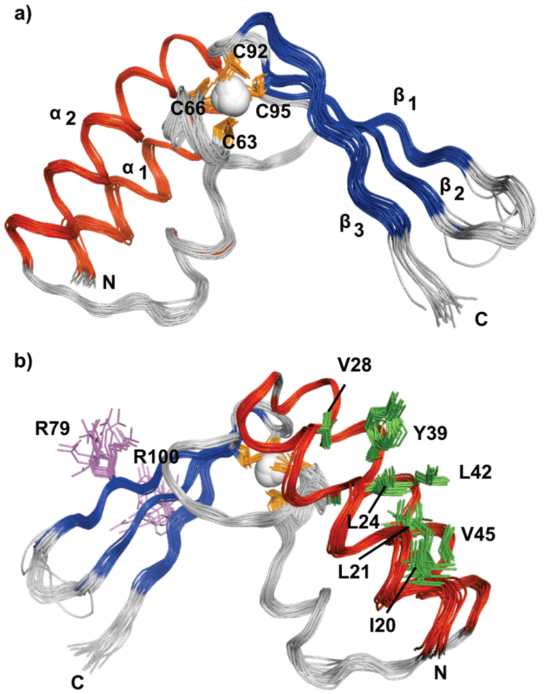

FIGURE 3: Solution structure of *Pfu* RPP21. (a) Ensemble of 20 lowest-energy structures superimposed on the backbone heavy atoms of residues 19−82 and 88−105. (b) Rotated view showing the side chains of some conserved residues.

Table 1: NMR Structural Statistics for *Pfu* RPP21

no. of NMR constraints	
NOE	1,352
intraresidue ($i - j = 0$)	515
sequential ($i - j = 1$)	381
short-range ($1 < i - j < 5$)	154
long-range ($i - j < 5$)	302
ambiguous	399
hydrogen bonds[a]	68
dihedral angles	158
no. of pseudocontact shifts (PCS)	169
no. of violations	
distance violations >0.5 Å	3.4 ± 2.0
dihedral angle violations >5°	0 ± 0
PCS violations	0 ± 0
deviation from idealized geometry	
bonds (Å)	0.003 ± 0.0003
angles (deg)	1.01 ± 0.05
impropers (deg)	8.1 ± 0.3
Ramachandran statistics[b] (%)	
favored region	96.6
disallowed region	0.0
precision (Å) (rmsd from the mean structure)	
backbone atoms	0.45
all heavy atoms	0.81

[a] Hydrogen bond restraints were applied as upper bound restraints between amide proton and oxygen atoms and between amide nitrogen and oxygen atoms. [b] Ramachandran analysis performed with MolProbity (*46*).

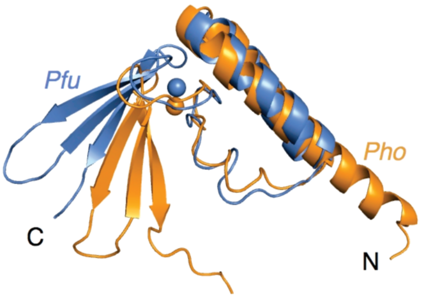

FIGURE 4: Superposition of *Pfu* and *Pho* RPP21. Superposition of the core structural elements of a representative member from the NMR ensemble and the X-ray structure.

HiTrap chelating column (GE Biosciences) charged with 100 mM nickel sulfate and equilibrated with denaturing loading buffer [50 mM Tris (pH 7.4), 50 mM KCl, 5 mM imidazole, and 8 M urea]. Second, fractions containing the protein were combined and purified by C4 reversed-phase HPLC (Vydac 214TP1010, 90 mL linear gradient from 30 to 60% acetonitrile). Then, the C-terminal (His)$_6$ tag was removed by incubation at 37 °C with thrombin (10 units/mg of *Pfu* RPP21) for 12 h, resulting in a 122-residue protein consisting of 116 natively encoded residues, without the N-terminal methionine, followed by six plasmid-encoded residues (Gly-Gly-Leu-Val-Pro-Arg). After cleavage of the affinity tag, the protein was purified form the peptide and protease by C4 reversed-phase HPLC chromatography, lyophilized, resuspended in denaturing buffer, and exchanged into NMR buffer [10 mM d_{11}-Tris (pH 6.7) at 25 °C, 10 mM KCl, 0.3 mM $ZnCl_2$, 0.02% sodium azide, and 10% D_2O] using a PD-10 gel filtration column (GE Healthcare). The cobalt-substituted RPP21 sample for measuring paramagnetic effects (below) was obtained by the same purification protocol, except that the pure lyophilized protein was refolded in buffer containing $CoCl_2$ instead of $ZnCl_2$. Protein purity and integrity were assessed by Coomassie Blue staining (Pierce) on SDS−PAGE gels and by electrospray mass spectrometry (Q-TOF II, Micromass, Inc.).

For the production of *Pfu* RPP29, the *Pfu* RPP29/pET-33b plasmid was transformed into *E. coli* Rosetta BL21(DE3) cells (Novagen), recombinant protein production was induced by addition of 1 mM IPTG when the cell density had reached an OD_{600} of ≈0.6, and the cells were harvested after 4 h by centrifugation. Cells were suspended in denaturing lysis buffer [25 mM Tris (pH 7), 7 M urea, 1 mM EDTA, and 10 mM DTT] and lysed by sonication. The protein was purified from the urea-solubilized lysate using a 5 mL HiTrap SP column equilibrated with lysis buffer. The protein was refolded on the column which was washed with 10 column volumes of buffer A [25 mM Tris (pH 7), 25 mM NaCl, and 1 mM DTT] and was eluted with a 60 mL linear gradient from 0.5 to 1.5 M NaCl. The purified protein was then dialyzed against *Pfu* RPP21 NMR buffer [10 mM Tris (pH 6.7), 10 mM KCl, 0.3 mM $ZnCl_2$, 1 mM DTT, and 0.02% NaN_3]. The protein concentration was estimated from the predicted extinction coefficient of 14770 M^{-1} cm^{-1} at 280 nm in denaturing buffer [50 mM phosphate (pH 7.5), and 6 M guanidinium hydrochloride] (*21*).

Limited Proteolysis. We subjected purified *Pfu* P21 (∼100 μM in NMR buffer) to limited proteolysis by adding 5% trypsin (w/w) and incubating the mixture at 37 °C for 1 h, and the reaction was quenched with 0.6 mM PMSF (Sigma). Partially proteolyzed samples were then analyzed by electrospray mass analysis (Q-TOF-II, Micromass).

NMR Spectroscopy and Resonance Assignments. Two-dimensional $^1H-^{15}N$ correlated NMR spectra of *Pfu* RPP21 recorded at 25 °C revealed many broad signals in the random coil chemical shift region of the spectrum (*22*), suggesting that portions of the protein had aggregated and/or were disordered at low temperatures. Nevertheless, NMR data recorded at 50 °C showed high-quality spectra with well-dispersed resonances. Thus, NMR data were collected at 50

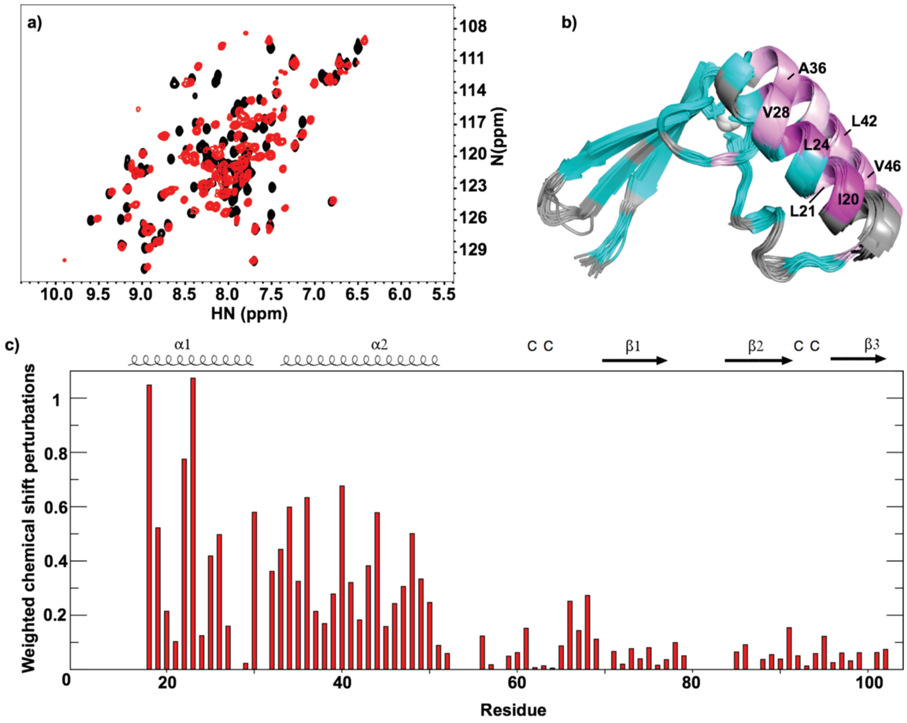

FIGURE 5: Binding of *Pfu* RPP21 to *Pfu* RPP29 as detected by NMR. (a) Overlay of ^{15}N HSQC spectra of *Pfu* RPP21 free (black) and *Pfu* RPP21 bound to *Pfu* RPP29 (red), illustrating the site-specific chemical shift perturbations that reveal the region of protein−protein interactions. (b) Binding-induced chemical shift perturbations mapped onto the ribbon diagram of RPP21: cyan, less than the mean perturbation; magenta, greater than mean. Residues for which the effect of RPP29 binding could not be determined are colored light gray. (c) Plot of weighted average chemical shift perturbations induced by protein−protein contacts.

°C on 600 and 800 MHz Bruker Avance DMX and DRX spectrometers equipped with triple-resonance triple-axis pulsed-field gradient probes. NMR data were processed and analyzed using NMRPipe (*23*), NMRView (*24*), CARA (*25*), and in-house scripts. The approximate concentration for RPP21 NMR samples was 1 mM, while concentrations of Co^{2+}-bound RPP21 and the RPP21−RPP29 complex were 0.5 mM.

Backbone resonance assignments for RPP21 free and in complex with RPP29 were obtained using standard triple-resonance spectra [HNCACB, HNCA, CBCA(CO)NH, and HNCO] (*26*) recorded at 600 MHz. Side chain resonance assignments were obtained from spectra recorded via ^{15}N-edited TOCSY-HSQC (*26*) (τ_m = 60 ms) at 800 MHz, HBHA(CBCACO)NH, CCONH-TOCSY (τ_m = 12 ms), three-dimensional (3D) HCCH-COSY (τ_m = 12 ms), and HCCH-TOCSY (τ_m = 12 ms) at 600 MHz (*26*). Distance restraints were obtained from 3D ^{15}N-edited NOESY-HSQC (τ_m = 200 ms) and ^{13}C-edited NOESY-HSQC (τ_m = 200 ms) spectra recorded in samples dissolved in 5 and 100% D_2O, respectively. Backbone resonance assignments for Co^{2+}-bound RPP21 were obtained using TROSY-based triple-resonance spectra (TROSY-HNCA, TROSY-HNCO, and TROSY-HNCACB) (*27*) recorded at 600 MHz and a 3D ^{15}N-edited NOESY-TROSY spectrum (*28*) (τ_m = 150 ms) recorded at 800 MHz.

Structure Determination. NOE-derived distance restraints from NOESY cross-peak intensities were calculated by assigning the median intensity an interproton distance of 2.7 Å and scaling the remaining intensities assuming a scaling of $\sim 1/r^6$, where r is the interproton distance (*24*). Restraints for methyl and non-stereo-assigned atoms were adjusted by adding 0.5 Å to the upper bound. Backbone torsion angle restraints were obtained from analysis of the H^N, N, C$^\alpha$, and C$^\beta$ chemical shifts with TALOS (*29*). Pseudocontact shifts (PCS) were calculated by comparing the H$^\alpha$, N, C$^\alpha$, C$^\beta$, and C′ chemical shifts between paramagnetic and diamagnetic spectra (*18, 30*).

Structure calculations for free *Pfu* RPP21 were performed using simulated annealing protocols within the XPLOR-NIH software suite (*31*), which includes a paramagnetism restraints module (*32*). An initial set of structures was generated using a small set of unambiguous long-range NOE restraints (~100), in addition to short-range NOE restraints and dihedral angle restraints. Paramagnetism-derived PCS restraints were introduced after estimation of the tensor (*32*). After each cycle, the structures obtained were used to calculate a new PCS tensor and used for iterative assignment of additional NOE cross-peaks. The zinc ion was linked to the four cysteines, modified to remove the H$^\gamma$, through upper distance restrains from C$^\beta$ (3.3 Å) and S$^\gamma$ (2.3 Å) atoms and used throughout the calculations. A final set of the 20 lowest-energy structures were selected from a set of 100 solutions and subsequently refined in explicit water (*33*) using restrained molecular dynamics in XPLOR-NIH (*31*). Analysis of structures was conducted using XPLOR-NIH (*31*), MolProbity (*46*) and PROCHECK-NMR (*34*). Structures and restraints have been deposited in the Protein Data Bank as entry 2K3R.

Identifying the RPP29 Binding Site of RPP21. The RPP29 interaction site on RPP21 was identified by examining the chemical shift differences between amide resonances of free and RPP29-bound U-[^{15}N]-RPP21 in two-dimensional ^{1}H−^{15}N correlated NMR spectra. Weighted average chemical shift perturbations were calculated from

$$\Delta\delta = |\Delta\delta_{HN}| + \frac{1}{a}|\Delta\delta_{N}|$$

where $a = 8$ for Gly and $a = 6$ otherwise (*19, 35*).

RESULTS

Pfu RPP21 Solution Structure. The ^{15}N-edited HSQC spectrum of *Pfu* RPP21 contains only 90 of the 115 expected backbone amide proton resonances (excluding the seven proline residues) (Figure 2a). This observation suggested that the N- and C-termini do not adopt a stable structure, consistent with sequence-based structural predictions (*36, 37*). Limited trypsin proteolysis experiments analyzed by mass spectrometry revealed two major proteolytic fragments with masses of 8635 and 11517 Da, corresponding to the expected masses of residues 37−108 (expected mass of 8632 Da) and 13−108 (expected mass of 11520 Da), respectively. The absence of significant cleavage of the remaining nine Lys or ten Arg residues suggested the presence of a well-structured central core between residues 13 and 108, with unstructured N- and C-termini beyond these bounds.

Backbone amide resonance assignments could be obtained for most of the signals observed in ^{15}N HSQC spectra, corresponding to 83% of the protease-resistant core of the protein (residues 13−108) and to 68% of all residues (Figure 2a). Residues that could not be assigned are 1−17, 56, 57, 60, 82−85, and 104−119, corresponding to regions located mainly in the N-terminus, a loop, and the C-terminus. Side chain assignments were determined for 81% of residues in the core (residues 13−108) and 66% for all the protein.

The effect of the paramagnetic cobalt metal on the ^{15}N HSQC spectrum is illustrated in Figure 2b. Due to the large chemical shift changes induced by the paramagnetic ion, backbone resonances for Co^{2+}-bound RPP21 had to be assigned de novo. Because of the enhanced relaxation rates of protein spins by the paramagnetic ion (*38*), the signals from residues in the immediate vicinity of the metal binding site were broadened beyond detection, and assignments could be obtained for only 49 residues of Co^{2+}-substituted RPP21. From these assignments, a total of 169 (H^N, N, C^α, and C^β) pseudocontact shifts (PCS) (*38*) could be obtained and were included in the structure calculations.

The solution structure of *Pfu* RPP21 is well-defined for the assigned residues (19−82 and 88−105), with mean root-mean-square deviations (rmsds) of 0.4 and 0.8 Å for backbone and heavy atoms, respectively (Figure 3); inclusion of the PCS restraints decreased the overall rmsds from 0.6 and 0.9 Å for backbone and heavy atoms, respectively. Although the PCS restraints had a modest effect on the precision of the structure, the longer-range information allowed for discrimination of alternative structures early during refinement. Overall, the structural quality is good, with 97% of the ψ and χ angles falling within the favored and additionally allowed regions of the Ramachandran plot (Table 1). The N-terminus of the structured region of the protein (residues 19−52) consists of two α-helices (α_1, residues 19−31, and α_2, residues 35−50), while the C-terminus of the protein (residues 57−105) adopts a zinc ribbon motif (*11, 39*) and consists of two hairpins providing the scaffold for the four invariant cysteine residues responsible for coordinating the zinc ion (Figure 3). The two α-helices dock against the open side of the zinc binding site of the zinc ribbon, protecting the metal from solvent.

Amino acid residues that are highly conserved across the RPP21 family decorate both the helical and zinc ribbon domains of the structure (Figure 1). The core is well-packed with highly conserved hydrophobic residues (not shown), with the three invariant hydrophobic residues (Leu21, Tyr39, and Ala43) forming part of the primary hydrophobic pocket keeping the helices together (Figure 3b). Of the three invariant arginine residues (Arg17, Arg79, and Arg100), the side chains of Arg79 and Arg100 are solvent-exposed (Figure 3b), while Arg17 is located in the disordered N-terminal region that precedes helix α_1. The pairings of several basic and acidic residues on the surface of the two helices (Glu16-Arg17, Glu26-Arg27, and Glu34-Arg38-Glu41) reveal a number of salt bridges that likely contribute to protein stability.

A crystal structure has been reported for *P. horikoshii* (*Pho*) RPP21 (*16*), which is 69% identical in sequence with *Pfu* RPP21. Superposition of the core structural elements (*Pfu* residues 17−103 and *Pho* residues 18−104) of a representative member from the NMR ensemble and the X-ray structure yields a rmsd of 3.3 Å. However, separate superposition of the α-helices (residues 18−49) and the zinc binding motif (residues 67−82 and 88−101) yields rmsds of 1.1 and 1.3 Å, respectively. Most of the structural difference between the *Pho* and *Pfu* structures lies in the linker (residue 51−62) that connects the N- and C-terminal regions, changing the relative orientation between the two α-helices and the zinc ribbon; although there was no evidence of flexibility in the NMR data, it seems likely that the precise geometry between the domains could vary. In addition, the first 13 residues of *Pfu* RPP21 were not seen to form a stable secondary structure in solution (at 50 °C), while for the crystal structure of *P. horikoshii* RPP21 (*16*), the N-terminal α-helix extended through this region of the protein (Figure 4).

RPP21 Binds to RPP29. Unlabeled RPP29 was titrated into solutions containing ^{15}N-labeled RPP21 to identify significant regions of interaction. NMR spectra of RPP21 partially saturated with RPP29 showed two sets of signals, indicating tight binding with dissociation being slow on the chemical shift time scale. Comparison of the ^{15}N HSQC spectra of *Pfu* RPP21 in the absence and presence of *Pfu* RPP29 reveals many chemical shift perturbations confirming the interactions suggested previously by yeast two-hybrid experiments (Figure 5) (*6, 7*). The addition of RPP29 in stoichiometric excess did not result in further changes in the HSQC sectrum of RPP21, consistent with a high-affinity 1:1 stoichiometry. The improvement in the signal-to-noise ratio and the reduction of overlap in the ^{15}N HSQC spectra of RPP21 when bound to RPP29 suggest that the protein is better folded when bound to its binary partner. Although some backbone resonance assignments could be inferred by comparing the ^{15}N HSQC spectra of the complex to those of free RPP21, large shift perturbations required reassignment of the backbone resonances of RPP21 it was when bound to RPP29. We obtained resonance assignments for all but residues 1−18, 56, 57, 60, 78−85, and 104−119. The largest backbone amide chemical shift perturbations induced by RPP29 are localized to the α-helices at the N-terminus of RPP21 (Figure 5b,c). A majority of the residues experiencing the largest amide shift perturbations are hydrophobic, in particular, Ile20, Leu21, Leu24, Ala25, Val28, Leu42, and Val46. In addition to hydrophobic residues, several charged (Arg27 and Arg38) and polar (Ser32) residues exhibited large shift perturbations. These chemical shift perturbations identify the RPP21−RPP29 interface (*19*).

DISCUSSION

While the exact functional role of each of the protein subunits of archaeal and eukaryotic RNase P remains to be determined, evidence suggests that at least some of the RNase P proteins function in pairs (*5, 7, 8, 40*) and contact either the RPR subunit (*41, 42*) or ptRNA substrate (*9*). An important step toward revealing the roles of the protein pairs is to understand their structure in solution and how they interact with the other components. The solution structure of *Pfu* RPP21 contains a structured central core (residues 15−105) and unstructured regions at both N- and C-termini. Both tails are highly populated by conserved basic residues that could help stabilize interactions with either the catalytic P RNA subunit or the substrate ptRNA through favorable electrostatic interactions.

The overall RPP21 protein fold is unique among family members (MMDB entry 35869) (*43*). The zinc ribbon domain that comprises residues ~60−104, however, is a common domain among nucleic acid binding proteins (*44*). As previously noted, this domain exhibits a high degree of similarity to archaeal and eukaryotic polymerase subunits exemplified by Rpb9 (*16*). Superposition of the zinc ribbon fold of RPP21 with that of Rpb9 from yeast RNA polymerase II positions the domain near the nucleic acid binding funnel (*45*), where its conserved arginine and lysine residues could make analogous contacts with nucleic acid substrates.

Chemical shift perturbations (Figure 5) induced by RPP29 clearly indicate that *Pfu* RPP21 forms a tight complex with *Pfu* RPP29 in the absence of the RPR. These perturbations indicate that the interaction is localized to the two α-helices of RPP21, which exhibit a number of exposed hydrophobic residues (Figures 3 and 5). Although increased signal dispersion was observed in the complex, no new resonances were observed for RPP21 upon binding RPP29, suggesting that no significant coupled folding of RPP21 occurs upon binding and that the protein−protein interaction involves the structured core RPP21. Such an interaction would leave the highly basic N- and C-terminal tails free to interact with either the RPR or the ptRNA.

Alanine scanning mutagenesis experiments directed at conserved residues in *Pho* RPP21 identified residues important for functional reconstitution (*16*). Those studies, although not quantitative, found that mutation to Ala of Arg17, Tyr39, Arg65, Arg81, and Arg100 (*Pfu* numbering) significantly impaired activity in the reconstituted enzyme, with the largest defects being associated with the Arg65 to Ala and Arg100 to Ala mutants. Given the location of Arg17 and Tyr39 in the NMR-identified interface with RPP29, we conclude that mutation of those residues might have impaired formation of the appropriate protein−protein contacts. On the other hand, Arg65 and Arg100 are located on the zinc ribbon motif, away from the RPP29 binding site. Yeast two-hybrid (*6−8*) and biophysical experiments (unpublished results) indicate little or no interaction between the RPP21−RPP29 and POP5−RPP30 protein pairs. Consequently, functional defects due to these RPP21 mutations implicate them and their associated molecular surfaces in binding either the RPR or ptRNA substrate.

This work has identified the molecular surface of RPP21 involved in binding RPP29, thereby informing the design of site-directed mutations aimed at probing interactions with the RNA subunit. Further studies will ascertain the details of how *Pfu* RPP21 interacts with RPP29 and how this complex interacts with other components of RNase P. Such studies should help reveal the function of the RPP21−RPP29 complex within the holoenzyme and allow further progress toward understanding assembly and function of this composite ribonucleoprotein enzyme.

ACKNOWLEDGMENT

We thank C. Yuan (CCIC) for assistance with NMR data collection, C. P. Jones (The Ohio State University) for help with sample preparation, and R. C. Wilson and members of the V. Gopalan laboratory for reagents, encouragement, and helpful discussions.

REFERENCES

1. Altman, S., Baer, M. F., Bartkiewicz, M., Gold, H., Guerrier-Takada, C., Kirsebom, L. A., Lumelsky, N., and Peck, K. (1989) Catalysis by the RNA subunit of RNase P: A minireview. *Gene 82*, 63–64.
2. Gopalan, V., and Altman, S. (2006) Ribonuclease P: Structure and Catalysis. In *The RNA World* (Gesteland, R., Cech, T., and Atkins, J., Eds.) Cold Spring Harbor Laboratory Press, Plainview, NY (available only online at http://rna.cshl.edu).
3. Evans, D., Marquez, S. M., and Pace, N. R. (2006) RNase P: Interface of the RNA and protein worlds. *Trends Biochem. Sci. 31*, 333–341.
4. Hall, T. A., and Brown, J. W. (2002) Archaeal RNase P has multiple protein subunits homologous to eukaryotic nuclear RNase P proteins. *RNA 8*, 296–306.
5. Tsai, H. Y., Pulukkunat, D. K., Woznick, W. K., and Gopalan, V. (2006) Functional reconstitution and characterization of *Pyrococcus furiosus* RNase P. *Proc. Natl. Acad. Sci. U.S.A. 103*, 16147–16152.
6. Jiang, T., and Altman, S. (2001) Protein-protein interactions with subunits of human nuclear RNase P. *Proc. Natl. Acad. Sci. U.S.A. 98*, 920–925.
7. Kifusa, M., Fukuhara, H., Hayashi, T., and Kimura, M. (2005) Protein-protein interactions in the subunits of ribonuclease P in the hyperthermophilic archaeon *Pyrococcus horikoshii* OT3. *Biosci., Biotechnol., Biochem. 69*, 1209–1212.
8. Hall, T. A., and Brown, J. W. (2004) Interactions between RNase P protein subunits in archaea. *Archaea 1*, 247–254.
9. Jarrous, N., Reiner, R., Wesolowski, D., Mann, H., Guerrier-Takada, C., and Altman, S. (2001) Function and subnuclear distribution of Rpp21, a protein subunit of the human ribonucleoprotein ribonuclease P. *RNA 7*, 1153–1164.
10. Mann, H., Ben-Asouli, Y., Schein, A., Moussa, S., and Jarrous, N. (2003) Eukaryotic RNase P: Role of RNA and protein subunits of a primordial catalytic ribonucleoprotein in RNA-based catalysis. *Mol. Cell 12*, 925–935.
11. Qian, X., Jeon, C., Yoon, H., Agarwal, K., and Weiss, M. A. (1993) Structure of a new nucleic-acid-binding motif in eukaryotic transcriptional elongation factor TFIIS. *Nature 365*, 277–279.
12. Boomershine, W. P., McElroy, C. A., Tsai, H.-Y., Wilson, R. C., Gopalan, V., and Foster, M. P. (2003) Structure of Mth11/Mth Rpp29, an essential protein subunit of archaeal and eukaryotic RNase P. *Proc. Natl. Acad. Sci. U.S.A. 100*, 15398–15403.
13. Wilson, R. C., Bohlen, C. J., Foster, M. P., and Bell, C. E. (2006) Structure of Pfu Pop5, an archaeal RNase P protein. *Proc. Natl. Acad. Sci. U.S.A. 103*, 873–878.
14. Kawano, S., Nakashima, T., Kakuta, Y., Tanaka, I., and Kimura, M. (2006) Crystal structure of protein Ph1481p in complex with protein Ph1877p of archaeal RNase P from *Pyrococcus horikoshii* OT3: Implication of dimer formation of the holoenzyme. *J. Mol. Biol. 357*, 583–591.

15. Takagi, H., Watanabe, M., Kakuta, Y., Kamachi, R., Numata, T., Tanaka, I., and Kimura, M. (2004) Crystal structure of the ribonuclease P protein Ph1877p from hyperthermophilic archaeon *Pyrococcus horikoshii* OT3. *Biochem. Biophys. Res. Commun. 319*, 787–794.
16. Kakuta, Y., Ishimatsu, I., Numata, T., Kimura, K., Yao, M., Tanaka, I., and Kimura, M. (2005) Crystal structure of a ribonuclease P protein Ph1601p from *Pyrococcus horikoshii* OT3: An archaeal homologue of human nuclear ribonuclease P protein Rpp21. *Biochemistry 44*, 12086–12093.
17. Banci, L., Piccioli, M., and Arnesano, F. (2005) NMR structures of paramagnetic metalloproteins. *Q. Rev. Biophys. 38*, 167–219.
18. Jensen, M. R., Hansen, D. F., Ayna, U., Dagil, R., Hass, M. A. S., Christensen, H. E. M., and Led, J. J. (2006) On the use of pseudocontact shifts in the structure determination of metalloproteins. *Magn. Reson. Chem. 44*, 294–301.
19. Foster, M. P., Wuttke, D. S., Clemens, K. R., Jahnke, W., Radhakrishnan, I., Tennant, L., Reymond, M., Chung, J., and Wright, P. E. (1998) Chemical shift as a probe of molecular interfaces: NMR studies of DNA binding by the three amino-terminal zinc finger domains from transcription factor IIIA. *J. Biomol. NMR 12*, 51–71.
20. Foster, M. P., McElroy, C. A., and Amero, C. D. (2007) Solution NMR of large molecules and assemblies. *Biochemistry 46*, 331–340.
21. Gasteiger, E., Hoogland, C., Gattiker, A., Duvaud, S., Wilkins, M. R., and Appel, R. (2005) *The Proteomics Protocols Handbook*, (Walker, J. M., Ed.) pp 571−607, Humana Press, Totowa, NJ.
22. Boomershine, W. P. (2005) Structure and Interactions of Archaeal RNase P Proteins Mth Rpp29 and Pfu Rpp21. Ohio State Biochemistry Program, The Ohio State University, Columbus, OH.
23. Delaglio, F., Grzesiek, S., Vuister, G. W., Zhu, G., Pfeifer, J., and Bax, A. (1995) NMRPipe: A multidimensional spectral processing system based on UNIX pipes. *J. Biomol. NMR 6*, 277–293.
24. Johnson, B. A. (2004) Using NMRView to visualize and analyze the NMR spectra of macromolecules. *Methods Mol. Biol. 278*, 313–352.
25. Keller, R. (2004) *The Computer Aided Resonance Assignment Tutorial*, CANTINA Verlag, Goldau.
26. Cavanagh, F. P. S. R. (2006) *Protein NMR Spectroscopy: Principles and Practice*, 2nd ed., Academic Press, New York.
27. Salzmann, M., Pervushin, K., Wider, G., Senn, H., and W,thrich, K. (1998) TROSY in triple-resonance experiments: New perspectives for sequential NMR assignment of large proteins. *Proc. Natl. Acad. Sci. U.S.A. 95*, 13585–13590.
28. Zhu, G., Kong, X., and Sze, K. (1999) Gradient and sensitivity enhancement of 2D TROSY with water flip-back, 3D NOESY-TROSY and TOCSY-TROSY experiments. *J. Biomol. NMR 13*, 77–81.
29. Cornilescu, G., Delaglio, F., and Bax, A. (1999) Protein backbone angle restraints from searching a database for chemical shift and sequence homology. *J. Biomol. NMR 13*, 289–302.
30. Bertini, I., Savellini, G. G., Romagnoli, A., Turano, P., Cremonini, M. A., Luchinat, C., Gray, H. B., and Banci, L. (1997) Pseudo-contact shifts as constraints for energy minimization and molecular dynamics calculations on solution structures of paramagnetic metalloproteins. *Proteins: Struct., Funct., Genet. 29*, 68–76.
31. Schwieters, C. D., Kuszewski, J. J., Tjandra, N., and Clore, G. M. (2003) The Xplor-NIH NMR molecular structure determination package. *J. Magn. Reson. 160*, 65–73.
32. Bertini, I., Cavallaro, G., Giachetti, A., Luchinat, C., Parigi, G., and Banci, L. (2004) Paramagnetism-Based Restraints for Xplor-NIH. *J. Biomol. NMR 28*, 249–261.
33. Spronk, C. A. E. M., Linge, J. P., Hilbers, C. W., and Vuister, G. W. (2002) Improving the quality of protein structures derived by NMR spectroscopy. *J. Biomol. NMR 22*, 281–289.
34. Laskowski, R. A., Rullmannn, J. A., MacArthur, M. W., Kaptein, R., and Thornton, J. M. (1996) AQUA and PROCHECK-NMR: Programs for checking the quality of protein structures solved by NMR. *J. Biomol. NMR 8*, 477–486.
35. Rooney, L. M., Sachchidanand, X., and Werner, J. M. (2004) Characterizing domain interfaces by NMR. *Methods Mol. Biol. 278*, 123–138.
36. Su, C.-T., Chen, C.-Y., and Hsu, C.-M. (2007) iPDA: Integrated protein disorder analyzer. *Nucleic Acids Res. 35*, W465–W472.
37. Ishida, T., and Kinoshita, K. (2007) PrDOS: Prediction of disordered protein regions from amino acid sequence. *Nucleic Acids Res. 35*, W460–W464.
38. Bertin, I., Luchinat, C., and Parigi, G. (2002) Magnetic susceptibility in paramagnetic NMR. *Prog. Nucl. Magn. Reson. Spectrosc. 40*, 249–273.
39. Qian, X., Gozani, S. N., Yoon, H., Jeon, C. J., Agarwal, K., and Weiss, M. A. (1993) Novel zinc finger motif in the basal transcriptional machinery: Three-dimensional NMR studies of the nucleic acid binding domain of transcriptional elongation factor TFIIS. *Biochemistry 32*, 9944–9959.
40. Pulukkunat, D. K., and Gopalan, V. (2008) Studies on *Methanocaldococcus jannaschii* RNase P reveal insights into the roles of RNA and protein cofactors in RNase P catalysis. *Nucleic Acids Res. 36*, 4172–4180.
41. Houser-Scott, F., Xiao, S., Millikin, C. E., Zengel, J. M., Lindahl, L., and Engelke, D. R. (2002) Interactions among the protein and RNA subunits of *Saccharomyces cerevisiae* nuclear RNase P. *Proc. Natl. Acad. Sci. U.S.A. 99*, 2684–2689.
42. Jiang, T., Guerrier-Takada, C., and Altman, S. (2001) Protein-RNA interactions in the subunits of human nuclear RNase P. *RNA 7*, 937–941.
43. Wang, Y., Addess, K. J., Chen, J., Geer, L. Y., He, J., He, S., Lu, S., Madej, T., Marchler-Bauer, A., Thiessen, P. A., Zhang, N., and Bryant, S. H. (2007) MMDB: Annotating protein sequences with Entrez's 3D structure database. *Nucleic Acids Res. 35*, D298–D300.
44. Krishna, S. S., Majumdar, I., and Grishin, N. V. (2003) Structural classification of zinc fingers: Survey and summary. *Nucleic Acids Res. 31*, 532–550.
45. Cramer, P., Bushnell, D. A., and Kornberg, R. D. (2001) Structural basis of transcription: RNA polymerase II at 2.8 angstrom resolution. *Science 292*, 1863–1876.
46. Davis, I. W., Leaver-Fay, A., Chen, V. B., Block, J. N., Kapral, G. J., Wang, X., Murray, L. W., Arendall, W. B., III, Snoeyink, J., Richardson, J. S., and Richardson, D. C. (2007) MolProbity: All-atom contacts and structure validation for proteins and nucleic acids. *Nucleic Acids Res. 35*, W375–W383.
47. Li, K.-B. (2003) ClustalW-MPI: ClustalW analysis using distributed and parallel computing. *Bioinformatics 19*, 1585–1586.
48. Gouet, P., Robert, X., and Courcelle, E. (2003) ESPript/ENDscript: Extracting and rendering sequence and 3D information from atomic structures of proteins. *Nucleic Acids Res. 31*, 3320–3323.

BI8015982